

Discovery of a nitrogen-enhanced metal-poor binary system: Possible evidence for pollution from an extinct massive AGB Star

José G. Fernández-Trincado^{1,2}, Ronald Mennickent³, Mauricio Cabezas⁴, Olga Zamora^{5,6}, Sarah L. Martell^{7,8}, Timothy C. Beers⁹, Vinicius M. Placco⁹, David M. Nataf¹⁰, Szabolcs Mészáros^{11,12}, Dante Minniti^{13,14,15}, Dominik R. G. Schleicher³, Baitian Tang¹⁶, Angeles Pérez-Villegas¹⁷, Annie C. Robin² and Céline Reylé²

(Affiliations can be found after the references)

Received ...; Accepted ...

ABSTRACT

We report the serendipitous discovery of a nitrogen-rich, mildly metal-poor ($[\text{Fe}/\text{H}] = -1.08$) giant star in a single-lined spectroscopic binary system found in the SDSS-IV Apache Point Observatory Galactic Evolution Experiment (APOGEE-2) survey, Data Release 14 (DR14). Previous work has assumed that the two percent of halo giants with unusual elemental abundances have been evaporated from globular clusters, but other origins for their abundance signatures, including binary mass transfer, must also be explored. We present the results of an abundance re-analysis of the APOGEE-2 high-resolution near-infrared spectrum of 2M12451043+1217401 with the Brussels Automatic Stellar Parameter (BACCHUS) automated spectral analysis code. Here, we verify the large N overabundance of 2M12451043+1217401 and re-determined the chemical abundances for a wider range of chemical species, including light and heavy elements. Our analysis confirms the N-rich nature of 2M12451043+1217401, which has a $[\text{N}/\text{Fe}]$ ratio of +0.69, and shows that the abundances of Al and Mg are mildly discrepant from that of a typical metal-poor RGB star, but exhibit C, Si, O and *s*-process abundances of typical field stars. We detect a particularly large variability in its radial velocity (RV) over the period of the APOGEE-2 observations, and the most likely orbit fit to the radial velocity data has a period of 730.89 ± 106.86 days, a velocity semi-amplitude of $9.92 \pm 0.14 \text{ km s}^{-1}$, and an eccentricity of $\sim 0.1276 \pm 0.1174$, which support the hypothesis of a binary companion. The present analysis shows a remarkable agreement between the observations and the theoretical yields from a likely massive ($5-7 \text{ M}_\odot$) asymptotic giant branch (AGB) star, which supports the idea that this star has been polluted in the past from an already extinct AGB companion, that is now possibly a white dwarf.

Key words. stars: abundances – stars: AGB and post-AGB – stars: evolution – stars: chemically peculiar — binaries: general – techniques: spectroscopic

1. Introduction

Today it is clear that stellar populations with distinctive light-element abundance patterns are extremely common in globular clusters (GCs), while metal-poor stars ($[\text{Fe}/\text{H}] \lesssim -0.7$) characterised by enhanced N ($[\text{N}/\text{Fe}] \gtrsim +0.5$) and depleted C ($[\text{C}/\text{Fe}] \lesssim +0.15$) are rarely found in the field (Johnson et al. 2007; Martell et al. 2011; Carollo et al. 2013). While currently still inconclusive, there is tantalising evidence that stars with "anomalous chemistry" may be present beyond GC environments (e.g., Lind et al. 2015; Fernández-Trincado et al. 2016b; Recio-Blanco et al. 2017).

To date, there have been a handful of stars fully characterised in terms of their chemistry and the chemical fingerprint of enriched *second population*¹ stars (e.g., Martell et al. 2016; Fernández-Trincado et al. 2016a, 2017; Schiavon et al. 2017), especially through observations of molecular ^{16}OH , $^{12}\text{C}^{14}\text{N}$ and $^{12}\text{C}^{16}\text{O}$ bands in the *H*-band of APOGEE (Majewski et al. 2017), which display the same chemical anomalies as stars in globular clusters, and exhibit conspicuous anomalies of the CNO elements, most notably N.

These nitrogen-enhanced stars (hereafter N-rich stars) have received significant attention in recent years, primarily because

they are believed to be likely relics of surviving Galactic and/or extragalactic (see Fernández-Trincado et al. 2017, for instance) globular clusters (Martell & Grebel 2010), or now fully dissolved globular clusters (Fernández-Trincado et al. 2015b,a; Reis et al. 2018), and as such, play an important role in deciphering the early history of the Milky Way itself.

A special feature of N-rich stars is their low carbon-abundance ratios, with all stars having $[\text{C}/\text{Fe}] \lesssim +0.15$ at $[\text{Fe}/\text{H}] \lesssim -0.7$, and characterised by significant star-to-star variations in the abundances of elements involved in proton-capture reactions, i.e., C, N, O, Mg, and Al.

Empirically, within the population of N-rich stars several subclasses exist, defined by their stellar metallicity and their Al and/or Mg abundances. Most of the N-rich stars in the bulge (e.g., Schiavon et al. 2017) exhibit intermediate aluminum ($[\text{Al}/\text{Fe}] \lesssim +0.25$) abundance ratios, similar to the thick disk. However, at higher metallicities, $[\text{Fe}/\text{H}] > -0.7$, Schiavon et al. (2017) identified a second group of N-rich stars chemically distinct from Milky Way stars across a variety of elements. Other groups of N-rich stars have been identified in the inner disk and the halo (Fernández-Trincado et al. 2016a, 2017), with $[\text{Al}/\text{Fe}] \gtrsim +0.5$, significantly above the typical Galactic level, across a range of metallicity. These stars are unlikely to have originated in tidally disrupted dwarf galaxies, because of the rarity of Al-rich stars in current dwarf galaxies (Shetrone et al. 2003; Hasselquist et al. 2017). Fernández-Trincado et al. (2017) found that some

¹ Here, we refer to the second population as the groups of stars showing enhanced N and Al, and depleted C and O abundances, with respect to other field stars at the same metallicity $[\text{Fe}/\text{H}]$.

N-rich field stars are also Mg-rich, similar to second-population stars in globular clusters, while some have a factor of two less Mg than field stars at the same metallicity. There is also a subclass of N-rich stars with lower Al abundances, $[\text{Al}/\text{Fe}] \lesssim +0.1$, which tend to follow halo-like orbits with very little net rotation (Martell et al. 2016).

The range of elemental abundances that can be derived from APOGEE H -band spectra makes it possible to identify and study these classes of stars in detail. With that information we can quantify their occurrence rates in the field, and study their overall kinematic properties, in order to better understand their origins.

The origins of most of these N-rich stars are currently under investigation, with theories ranging from the formation of a N-rich star via AGB companion mass transfer or a massive evolved massive star, as suggested by (Lennon et al. 2003), where the former AGB companion has since become a faint white dwarf (see Pereira et al. 2017), to early accretion of GCs or dwarf spheroidal galaxies (dSPhs), as such stars appear chemically distinguishable from disk/halo/bulge stars. However, the dynamical history of such stars remains unexplored to date. Measuring additional properties of the N-rich stars may help to further distinguish among them, provide clues to their origins, and/or identify more sub-populations, or more broadly help to understand GC formation and evolution.

In this study, we present the serendipitous discovery of a N-rich star confirmed to be in a binary system with a compact object. The new object associated to 2M12451043+1217401 is a nitrogen-enhanced and carbon-depleted metal-poor star with abundances of Al and Mg mildly discrepant from that of normal RGB stars. We hypothesise that this star is likely to be an example of the result of mass transfer from a binary companion, which is now in the white dwarf stage of stellar evolution. The discovery of such stars helps guide models that attempt to explain the unusual elemental abundances over a wide range of metallicities.

This paper is outlined as follows. In Section 2, we present details and information regarding our serendipitous discovery in the APOGEE-2 dataset. In Section 3, we describe and discuss the behaviour of the measured light and heavy elements. In Section 4, we present our main conclusions.

2. Data

For our analysis we make use of the publicly available H -band spectra from the APOGEE-2 survey (Majewski et al. 2017). We draw on the latest data release, DR14 (Abolfathi et al. 2018), obtained with the multi-object high-resolution spectrograph APOGEE mounted at the Sloan 2.5m Telescope (Gunn et al. 2006) at Apache Point Observatory, which began observation in 2014 as part of the Sloan Digital Sky Survey IV (Blanton et al. 2017). A detailed description of these observations, targeting strategy, data reduction, and APOGEE stellar-parameter estimates can be found in Zasowski et al. (2013), Zasowski et al. (2017), Nidever et al. (2015), Holtzman et al. (2015), Zamora et al. (2015) and García Pérez et al. (2016), respectively.

We start by searching for high-[N/Fe] outliers in the [N/Fe]-[Fe/H] abundance space in the first Payne data release of APOGEE abundances (see Ting et al. 2018, hereafter Payne-APOGEE). The Payne routine simultaneously derives best-fit values for all atmospheric parameters and abundances using neural networks, with the parameter space of the training set restricted to $[\text{Fe}/\text{H}] \gtrsim -1.5$. For each source, it only reports values for the measurement with the highest SNR.

The sample was then restricted to the metallicity regions $-1.5 \lesssim [\text{Fe}/\text{H}] \lesssim -0.7$, and giant stars with $\log g < 3.6$, which encompasses the transition between the Galactic thick disk and halo, following the same line of investigation as in Fernández-Trincado et al. (2017). Thus, we adopt the atmospheric parameters and $[\text{C}, \text{N}, \text{O}/\text{Fe}]$ and $[\text{Fe}/\text{H}]$ abundance ratios reported in the Payne catalog as the first-guess input parameters into the Brussels Automatic Stellar Parameter (BACCHUS) code (Masseron et al. 2016) in order to derive the metallicity and chemical abundances reported in Table 1. In addition to those literature values, we also systematically synthesised every element and line of 2M12451043+1217401 at high spectral resolution, to compare with the Payne and ASPCAP determinations. We have made careful line selection, as well as providing abundances based on a line-by-line differential approach in the atomic and molecular input data. The abundances that are derived for 2M12451043+1217401 using BACCHUS, found in Table 1, are generally in good agreement with those in the literature. In Appendix A, we describe the BACCHUS pipeline in more detail.

Table 1. Comparison of the mean elemental abundances derived from our target 2M12451043+1217401 using the “abund” module in BACCHUS code, and those obtained with the Payne and ASPCAP pipeline.

Element	BACCHUS [†]		Payne	ASPCAP
	Masseron et al. (2016)	Ting et al. (2018)	García Pérez et al. (2016)	
T_{eff}	4750.2 \pm 100 K	4750.2 K	4886.9 \pm 92.7 K	
$\log g$	2.24 \pm 0.3	2.24	2.22 \pm 0.08	
ξ_t	1.86 \pm 0.05 km s $^{-1}$	1.39 km s $^{-1}$	1.44 km s $^{-1}$	
$[\text{Fe}/\text{H}]$	-1.08 \pm 0.14	-1.09	-1.12 \pm 0.01	
$[\text{C}/\text{Fe}]$	0.06 \pm 0.24	-0.23	-0.13 \pm 0.07	
$[\text{N}/\text{Fe}]$	0.69 \pm 0.22	0.66	0.74 \pm 0.09	
$[\text{O}/\text{Fe}]$	0.46 \pm 0.23	0.22	0.22 \pm 0.07	
$[\text{Al}/\text{Fe}]$	0.04 \pm 0.16	-0.04	-0.05 \pm 0.08	
$[\text{Mg}/\text{Fe}]$	0.10 \pm 0.14	0.22	0.22 \pm 0.04	
$[\text{Si}/\text{Fe}]$	0.22 \pm 0.12	0.28	0.21 \pm 0.04	
$[\text{Ce}/\text{Fe}]$	<0.48 \pm 0.20	

Notes. The reported uncertainty for each chemical species in column 2 is: $\sigma_{\text{total}} = \sqrt{\sigma_{[\text{X}/\text{H}], T_{\text{eff}}}^2 + \sigma_{[\text{X}/\text{H}], \log g}^2 + \sigma_{[\text{X}/\text{H}], \xi_t}^2 + \sigma_{\text{mean}}^2}$. The Solar reference abundances are from Asplund et al. (2005). [†]The BACCHUS pipeline was used to derive the broadening parameters, metallicity, and chemical abundances.

The high-[N/Fe] outlier sample itself was defined by fitting a 5th order polynomial to the run of [N/Fe] with [Fe/H] and taking stars deviating from the fit by $+2.5\sigma$. 2M12451043+1217401 is a high-[N/Fe] outlier in chemical space, as compared to the bulk of the disk, bulge, and halo stars in the Payne-APOGEE sample. The sample in Fig. 1 contains stars with $[\text{C}/\text{Fe}] < +0.15$, because higher [C/Fe] abundance ratios are not typically found in globular clusters, and we want to avoid contamination by CH stars, for instance.

In this first work, we have only analysed one star (2M12451043+1217401), with large variability in radial velocity, out of 35 high-[N/Fe] outliers recently identified in Fernández-Trincado et al., (2019, in prep.), who analysed the same data set. The reader solely interested in the discussion of variability may see Appendix B and skip the latter sections. While a comprehensive analysis of our new high-[N/Fe] outliers

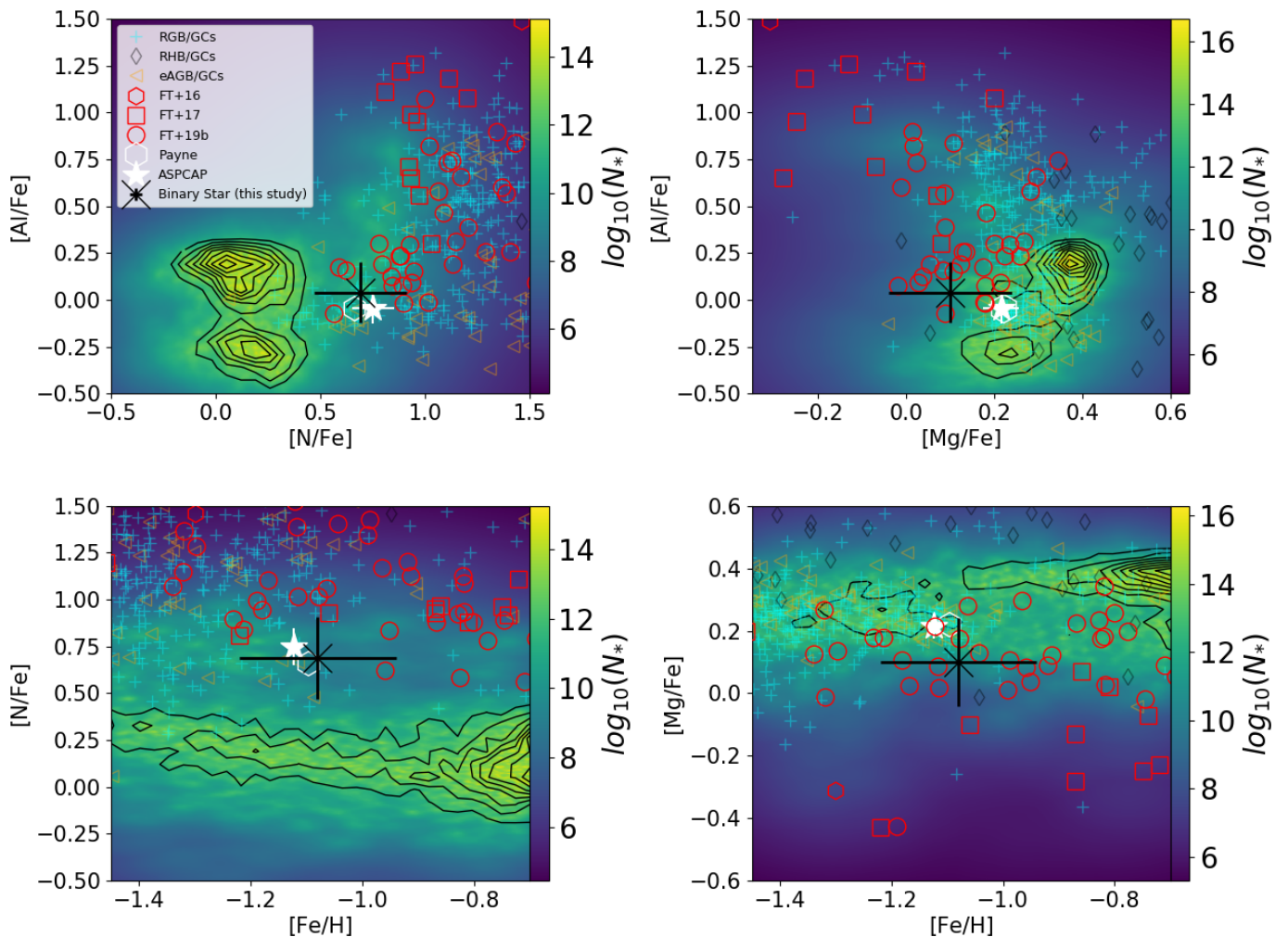


Fig. 1. The background color in each panel shows a Kernel Density Estimate (KDE) smoothed distribution of $[\text{Mg/Fe}]$, $[\text{Al/Fe}]$, $[\text{N/Fe}]$, and $[\text{Fe/H}]$ of Payne-APOGEE stars, while the black contours show the density of stars with "normal" N abundance ($\lesssim +0.5$), and highlighted with a black symbol is the new N-rich star, 2M12451043+1217401 (see text). The plotted error bar shows the classical standard deviation derived from the different abundances of the different lines for each element, as reported in Table 1. The same field sample is compared to APOGEE determinations for RGB, eAGB, and RHB stars (orange symbols) in GCs, M13 ($[\text{Fe/H}] = -1.53 \pm 0.04$), M3 ($[\text{Fe/H}] = -1.50 \pm 0.05$), M5 ($[\text{Fe/H}] = -1.29 \pm 0.02$), M107 ($[\text{Fe/H}] = -1.02 \pm 0.02$) and M71 ($[\text{Fe/H}] = -0.78 \pm 0.02$) from (Masseron et al. 2018), and a sample of known N-rich stars plotted using small cyan symbols: M16—Martell et al. (2016) and S17—Schiavon et al. (2017) from Payne-APOGEE abundances, and FT16—Fernández-Trincado et al. (2016a) and FT17—Fernández-Trincado et al. (2017) from a line-by-line differential analysis.

is beyond the scope of this paper, we did search in the literature for other high-[N/Fe] outliers in the more metal-poor ($[\text{Fe/H}] \lesssim -0.7$) population, identified in the APOGEE sample by Martell et al. (2016), Schiavon et al. (2017), and Fernández-Trincado et al. (2016a, 2017), with available chemical abundances in the Payne-APOGEE catalog, to verify that both Payne-APOGEE abundances and the polynomial fit used in this work is properly returning high-[N/Fe] outliers by recovering the most obvious known nitrogen-enhanced population. The results of this comparison are shown in the left-bottom panel of Fig. 1.

Figure 2 displays an example for a portion of the observed APOGEE spectrum of 2M12451043+1217401, where the $^{12}\text{C}^{14}\text{N}$ absorption feature is quite strong. As a comparison, we also show the APOGEE spectrum of a field star with a "normal" nitrogen abundance ($[\text{N/Fe}] \lesssim +0.5$), 2M15182930+0206378, with stellar parameters and metallicity

identical to that of the N-rich star. The N-rich star has remarkably stronger $^{12}\text{C}^{14}\text{N}$ lines, which can only mean that it has much higher nitrogen abundance. We conclude that the nitrogen abundance reported here, which is the basis for our identification of a new high-[N/Fe] outlier in the Milky Way, is highly reliable, and detectable in 2M12451043+1217401.

3. Stellar parameters and chemical-abundance measurements

The first estimates for stellar parameters for 2M12451043+1217401 we adopted in the present work are (T_{eff} , $\log g$, ξ_t , $[\text{M/H}]$) = (4750.2 K, 2.24, 1.86 km s^{-1} , -1.09), taken from Payne-APOGEE catalogue. With this set

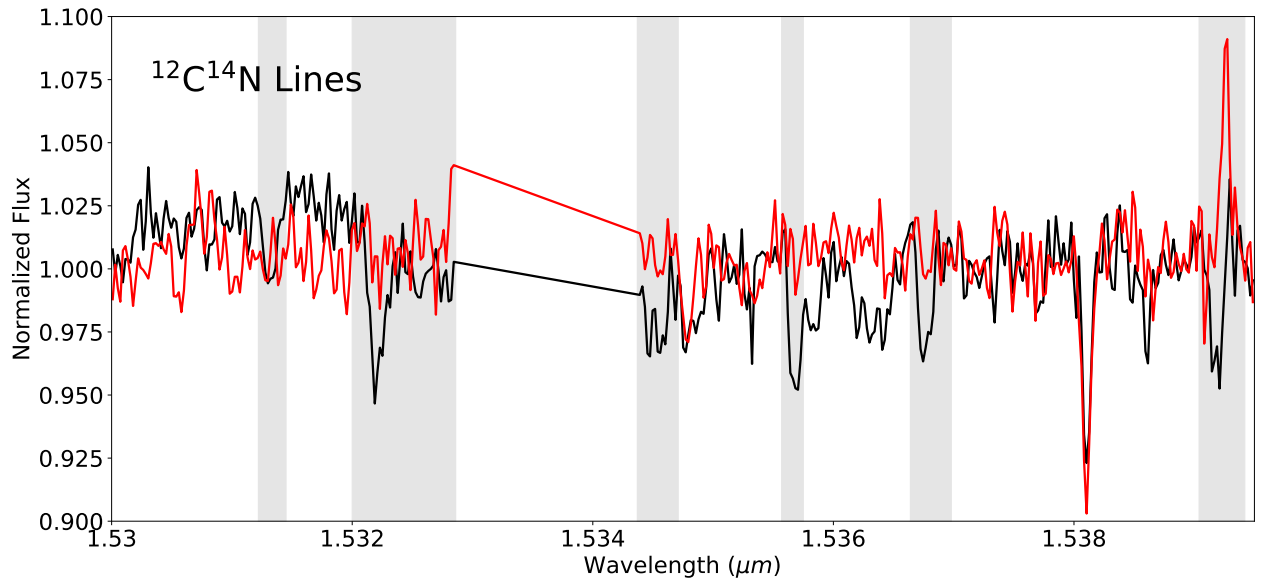


Fig. 2. Comparison between the spectrum of a normal (red) and our N-rich star (black), with similar stellar parameters and similar metallicity. The gray vertical bands indicate the positions of $^{12}\text{C}^{14}\text{N}$ lines.

of parameters, we performed an abundance analysis using the LTE abundance code BACCHUS (Masseron et al. 2016), using the plane-parallel, one dimensional grid of MARCS model atmospheres (Gustafsson et al. 2008). The results are listed in Table 1. The metallicity listed in column 2 of Table 1 is the average abundance of selected Fe I lines, and is in acceptable agreement with that determined from the ASPCAP and Payne-APOGEE pipelines.

Here, we explore whether or not our chemical-abundance measurements have the ability to chemically tag stars associated with globular clusters by performing a weak chemical-tagging analysis. Because we are interested in searching for high-[N/Fe] outliers with chemical signatures typical of globular cluster members, we focus on the abundances of C, N, O, Si, Mg, and Al. We have also attempted to measure one additional element, namely Ce II, because it has detected lines in the 2M12451043+1217401 spectrum. However, those lines are weak and, in some cases, heavily blended, thus the derived abundances strongly depend on our ability to properly reproduce the blend. At this time, we cannot guarantee the quality of the abundances for this element. However, Ce II presents three promising and strong lines (15784.8, 15958.4 and 16376.5 Å). This full set of abundance will be the basis of our comparison with the literature values.

3.1. Light-elements via spectrum synthesis: ^{16}OH , $^{12}\text{C}^{16}\text{O}$, $^{12}\text{C}^{14}\text{N}$, Mg I, Al I, and Si I lines

To put our results in context, we combined the chemical-abundance patterns ([Fe/H], [N/Fe], [Mg/Fe], and [Al/Fe]) of 2M12451043+1217401, along with the chemical-abundance pattern of globular cluster stars, other unusual giant stars (e.g., Martell et al. 2016; Fernández-Trincado et al. 2016a, 2017; Schiavon et al. 2017) from the APOGEE survey, and the entire Milky Way sample, see Fig. 1.

It is immediately clear from Fig. 1 that the chemical-abundance pattern of 2M12451043+1217401 appears to be dis-

tinguishable from Galactic populations. Similarly, its elevated [N/Fe] and low [C/Fe] ratio, as well as the chemical distribution in the α -elements, appear most similar to those seen in the chemistry of normal stars in GCs (often called first-generation stars), and comparable to a few nitrogen-enhanced metal-poor field stars at similar metallicity. On the other hand, the moderately enhanced nitrogen level of this star, [N/Fe] $\sim +0.69$, suggests that this value is above the boundary that separates N-rich stars ([N/Fe] $\gtrsim +0.5$) from objects with "normal" N abundances ([N/Fe] $\lesssim +0.5$), according to our strategy to separate these two population (see above text). This is strongly manifested in the [Fe/H] vs. [N/Fe] plane in Fig. 1.

In [Fe/H] and [N/Fe] abundances, this star most closely resembles globular cluster stars and the nitrogen-enhanced metal-poor field stars discussed in Schiavon et al. (2017), and the low [C/Fe] ~ -0.06 suggests that a significant fraction of the star's initial carbon has been converted to nitrogen via the CN(O) cycle. Another possible source for the abundance pattern in 2M12451043+1217401, given its radial velocity variability, is binary mass transfer from a massive ($M \sim 5 - 7 M_{\odot}$) AGB companion (see, e.g., Starkenburg et al. 2014). The mass range for the donor star is determined by the minimum mass for the third dredge-up, and by the onset of effective hot bottom burning, which burns C into N quite effectively.

The similarity between 2M12451043+1217401 and first-population stars from globular clusters can be further tested through examination of other chemical abundances typically found in GCs. As can be seen in Fig. 1, this star occupies the same region of Mg-Al abundance space as first-population globular cluster stars, without strong evidence of MgAl cycles. The Si abundance is also moderately enriched, which is typical for globular clusters. While the abundance pattern of 2M12451043+1217401 is consistent with first-population globular cluster stars, it is distinct from the overall APOGEE data set, which contains bulge, disk and halo stars.

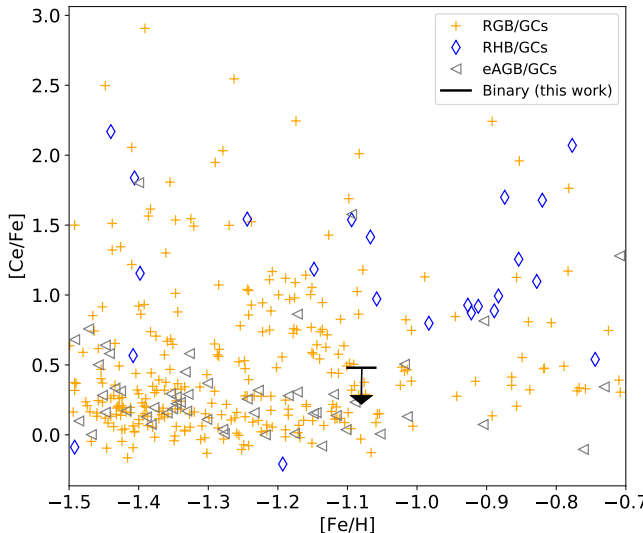


Fig. 3. Abundances of [Fe/H] vs. [Ce/Fe] in a large number of Galactic globular cluster stars (M107, M71, M5, M3 and M13) from Masseron et al. (2018). The N-rich binary star (2MASS J12451043+1217401) with estimated Ce II upper limit is indicated by an arrow symbol.

3.2. Neutron-capture elements via spectrum synthesis: Ce II lines

Here, from spectral synthesis of the Ce II lines in the APOGEE window, at 15784.8, 15958.4 and 16376.5 Å, we derived an upper limit to the cerium abundance ratio of $[Ce/Fe] = +0.48 \pm 0.20$, with an uncertainty mainly driven by stellar parameters (see Table A.3), mostly sensitive to the surface gravity. For more details on the method adopted to compute upper limits of abundances with the BACCHUS code, see Masseron et al. (2018).

The presence of normal neutron-capture elements (Ce II), which is in the heavy second *s*-process peak, indicates that the binary companion was likely to be a $5-7 M_{\odot}$ AGB star. Previous studies of Ce abundance in the Galaxy support the notion that *s*-process elements are synthesized in AGB stars, where a reaction occurs in freshly synthesized ^{13}C ($^{13}\text{C}(\alpha, n)^{16}\text{O}$) that results in a steady flux of neutrons. In more massive AGB stars, the higher temperature $^{22}\text{Ne}(\alpha, n)^{25}\text{Mg}$ reaction is activated and also contributes, and may become the dominant source of neutron flux (cf. Hasselquist et al. 2016) and (García-Hernández et al. 2006; Sneden et al. 2008; Bisterzo et al. 2011; Starkenburg et al. 2014; Hasselquist et al. 2016; Hansen et al. 2016). We also agree that the upper limit for Ce in 2MASS J12451043+1217401 is comparable to that of globular cluster RGB and eAGB stars (Masseron et al. 2018) at the same metallicity, as illustrated in Figure 3. Even though Masseron et al. (2018) concluded that polluters in a few of these GCs do not produce Ce abundance ratios with a possible origin in the cluster's primordial formation gas, here we find by the tell-tale radial-velocity variations that AGB stars are by far the most likely culprits for the pollution of our star beyond the GC environment.

We have shown that 2MASS J12451043+1217401 does show RV variation, which is consistent with being a binary. It is indeed possible that a companion of mass between 5 and $7 M_{\odot}$ has un-

dergone its AGB phase and dumped shell-nucleosynthesis processed material onto the observed star, in a similar fashion to what happens for CH and CEMP stars (e.g., Cristallo et al. 2016), increasing the content of N as well as a mildly enhanced value of $[Ce/Fe] \lesssim +0.48$.

These new C, N, O, Si, Mg, Al, and Ce abundances are then compared with AGB nucleosynthesis theoretical predictions: FRUITY² models from Cristallo et al. (2015), which we have compared observations with the FRUITY models of metallicity $Z = 1 \times 10^{-3}$, $Z = 2 \times 10^{-3}$, and $Z = 3 \times 10^{-3}$, Monash model of metallicity $[Fe/H] = -1.2$ from Fishlock et al. (2014) and ATON model ($[Fe/H] = -1.2$) from Ventura et al. (2016) as shown in Figure 4. The reason is that the RGB (2MASS J12451043+1217401) from this binary system is expected to be polluted by a former AGB companion, thus their atmospheric chemistry must reflect the yields from an AGB star. Basically, we find that our reference theoretical FRUITY and Monash set fits only part of the observations, in particular regarding C, N, Mg, Al, Si, and Ce, and give support to the hypothesis that the process responsible for the star (with a possible white dwarf remnant companion) in this study and polluted material transferred from a former massive AGB binary companion, are related. Therefore the AGB progenitor that is responsible for the signal is most likely in the range of $M \sim 5 - 7 M_{\odot}$, but not more massive than $7 M_{\odot}$. It is important to note that deviation presented by some species, such as O may be due to the fact that abundance of $[O/Fe]$ is uncertain in this T_{eff} regime studied here. The uncertainty arises because $[O/Fe]$ is determined from the strength of $^{12}\text{C}^{16}\text{O}$ lines, which become too weak for $T_{\text{eff}} \gtrsim 4500$ K at relatively low metallicities ($[Fe/H] \lesssim -1$), see Mészáros et al. (2015) and Schiavon et al. (2017).

4. Concluding remarks

In this work, we communicate the serendipitous discovery of an unusual red-giant star that shows significantly enhanced $[N/Fe]$ and possibly depleted $[C/Fe]$ abundance ratios among metal-poor field stars. Based on high-resolution NIR spectroscopic data from the APOGEE-2 survey, we determined the atmospheric parameters, spectroscopic distance, radial velocity variability, abundances of light elements (C, N, O, Mg, Al and Si), and the elements created by the *s*-process (Ce II) for 2MASS J12451043+1217401.

Combining the large radial velocity variation, no carbon enrichment, and nitrogen over-abundance, we hypothesize that an AGB-binary system may produce a $[N/Fe]$ over-abundance in some N-rich stars within the Milky Way, since mass transfer happened in the past, and the star is a normal RGB star where we see the effects due to the pollution of a companion of mass between 5 and $7 M_{\odot}$ that has undergone its AGB phase and dumped shell-nucleosynthesis processed material onto the observed star, i.e., the AGB companion deposits its N-rich outer layers onto its RGB companion through accreting winds, the binary system produces N (destroying C in the process), that is then mixed throughout the RGB envelope. The companion star in the system is now a possible white dwarf.

A dynamical study of 2MASS J12451043+1217401 shows that this system has a retrograde motion with a highly eccentric orbit, consistent with the Galactic inner halo population. The results are described in Appendix C and illustrated in Figure C.1. By

² Full-Network Repository of Updated Isotopic Tables and Yields: <http://fruity.oa-abruzzo.inaf.it/>.

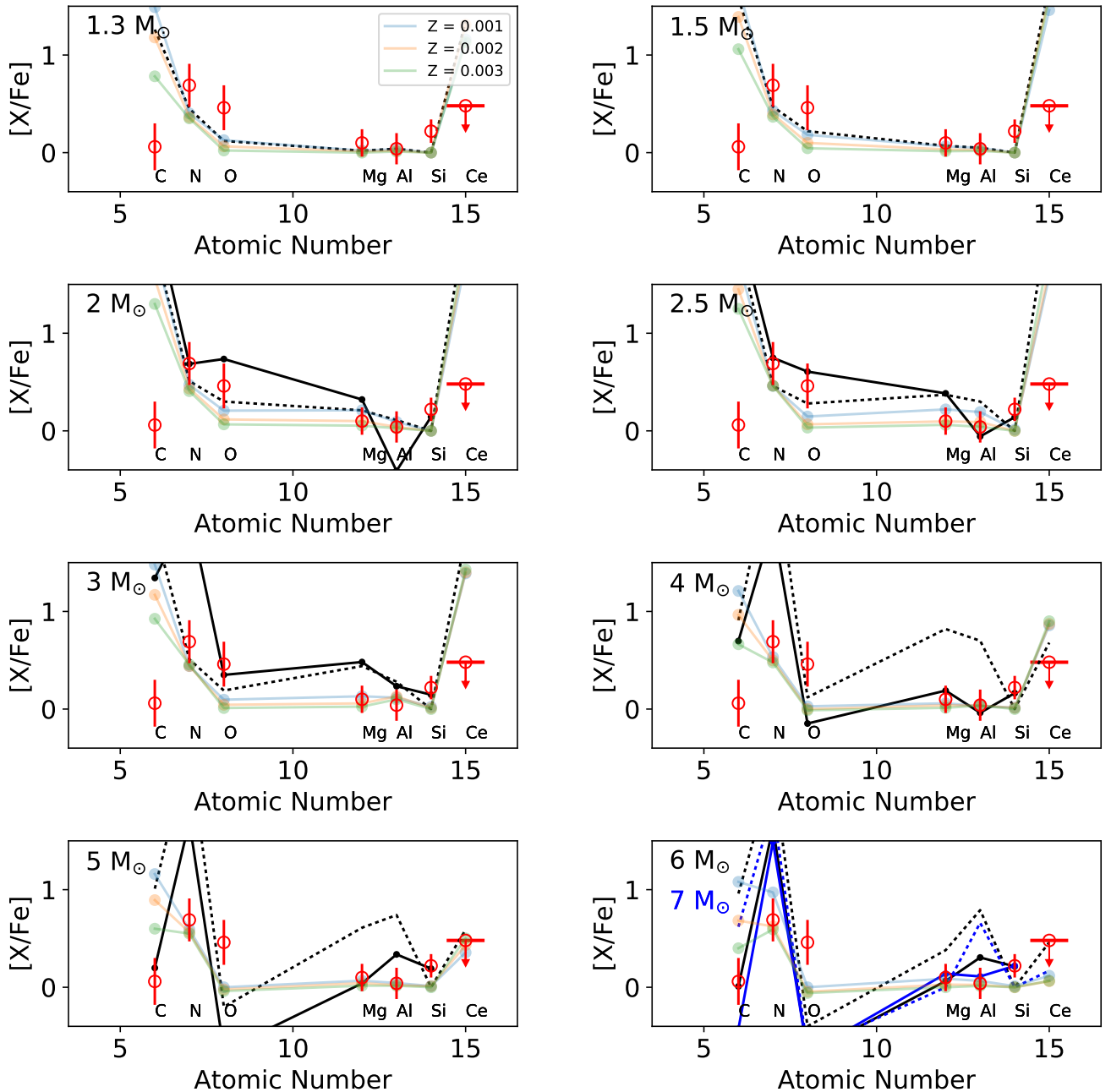


Fig. 4. Chemical abundance distribution vs. atomic number of the mildly metal-poor binary star, 2M12451043+1217401 (red open circles, arrow for an upper limit). The abundances are compared to AGB star models at different metallicities from FRUITY (cyan, orange and green lines), Monash (black and blue dotted lines) and ATON (black and blue continuum lines). The dash-dotted line shows the solar abundance ratios for comparison. Elements and upper abundance limits are indicated. The atomic number of Ce was shifted for better illustration of the data. The mass of each theoretical FRUITY model is shown in the inner left corner.

this we mean that this system was formed early on before the inner halo formation, or else, the system formed together with the inner-halo, indicating that stripped or destroyed globular clusters need not be a significant source of inner-halo field stars. The present paucity of halo N-enriched stars could therefore also have implications for the binary fraction in the field, which to date has been difficult to determine. This study further supports the idea that massive AGB stars could be the key play-

ers in the pollution of $^{12}\text{C}^{14}\text{N}$ via a slow stellar wind which has polluted the RGB, thus their atmospheric chemistry reflect the yields from an AGB star.

Acknowledgements. We thank Jesús Hernández, Aníbal García Hernández, Paolo Ventura, Thomas Masseron and Diogo Souto for helpful comments and support. J.G.F-T is supported by FONDECYT No. 3180210 and the European COST Action CA16117 (ChETEC) project No 41736. R.E.M. gratefully acknowledges support by VRID-Enlace 218.016.004-1.0 and the Chilean Cen-

tro de Excelencia en Astrofísica y Tecnologías Afines (CATA) BASAL grant AFB-170002. M.C. acknowledges support by Astronomical Institute of the Czech Academy of Sciences through the project RVO 67985815. O.Z. acknowledge support by the MINECO under grant AYA-2017-88254-P. SzM has been supported by the Premium Postdoctoral Research Program of the Hungarian Academy of Sciences, and by the Hungarian NKFI Grants K-119517 and GINOP-2.3.2-15-2016-00003 of the Hungarian National Research, Development and Innovation Office. D.M. acknowledges support from FONDECYT Regular grant No. 1170121, and the kind hospitality of the Osservatorio di Capodimonte/INAF, Italy. T.C.B. and V.M.P. acknowledge partial support for this work from grant PHY 14-30152; Physics Frontier Center / JINA Center for the Evolution of the Elements (JINA-CEE), awarded by the US National Science Foundation. Funding for the GravPot16 software has been provided by the Centre national d'études spatiales (CNES) through grant 0101973 and UTINAM Institute of the Université de Franche-Comté, supported by the Région de Franche-Comté and Institut des Sciences de l'Univers (INSU). Simulations have been executed on computers from the Utinam Institute of the Université de Franche-Comté, supported by the Région de Franche-Comté and Institut des Sciences de l'Univers (INSU), and on the supercomputer facilities of the Mésocentre de calcul de Franche-Comté. Funding for the Sloan Digital Sky Survey IV has been provided by the Alfred P. Sloan Foundation, the U.S. Department of Energy Office of Science, and the Participating Institutions. SDSS-IV acknowledges support and resources from the Center for High-Performance Computing at the University of Utah. The SDSS web site is www.sdss.org. SDSS-IV is managed by the Astrophysical Research Consortium for the Participating Institutions of the SDSS Collaboration including the Brazilian Participation Group, the Carnegie Institution for Science, Carnegie Mellon University, the Chilean Participation Group, the French Participation Group, Harvard-Smithsonian Center for Astrophysics, Instituto de Astrofísica de Canarias, The Johns Hopkins University, Kavli Institute for the Physics and Mathematics of the Universe (IPMU) / University of Tokyo, Lawrence Berkeley National Laboratory, Leibniz Institut für Astrophysik Potsdam (AIP), Max-Planck-Institut für Astronomie (MPIA Heidelberg), Max-Planck-Institut für Astrophysik (MPA Garching), Max-Planck-Institut für Extraterrestrische Physik (MPE), National Astronomical Observatory of China, New Mexico State University, New York University, University of Dame, Observatório Nacional / MCTI, The Ohio State University, Pennsylvania State University, Shanghai Astronomical Observatory, United Kingdom Participation Group, Universidad Nacional Autónoma de México, University of Arizona, University of Colorado Boulder, University of Oxford, University of Portsmouth, University of Utah, University of Virginia, University of Washington, University of Wisconsin, Vanderbilt University, and Yale University.

References

Abolfathi, B., Aguado, D. S., Aguilar, G., et al. 2018, *ApJS*, 235, 42

Alvarez, R. & Plez, B. 1998, *A&A*, 330, 1109

Asplund, M., Grevesse, N., & Sauval, A. J. 2005, in Astronomical Society of the Pacific Conference Series, Vol. 336, Cosmic Abundances as Records of Stellar Evolution and Nucleosynthesis, ed. T. G. Barnes, III & F. N. Bash, 25

Bailer-Jones, C. A. L., Rybizki, J., Fouesneau, M., Mantelet, G., & Andrae, R. 2018, *AJ*, 156, 58

Bisterzo, S., Gallino, R., Straniero, O., Cristallo, S., & Käppeler, F. 2011, *MNRAS*, 418, 284

Blanton, M. R., Bershady, M. A., Abolfathi, B., et al. 2017, *AJ*, 154, 28

Brunthaler, A., Reid, M. J., Menten, K. M., et al. 2011, *Astronomische Nachrichten*, 332, 461

Carollo, D., Martell, S. L., Beers, T. C., & Freeman, K. C. 2013, *ApJ*, 769, 87

Charbonneau, P. 1995, *ApJS*, 101, 309

Cristallo, S., Karinkuzhi, D., Goswami, A., Piersanti, L., & Gobrecht, D. 2016, *ApJ*, 833, 181

Cristallo, S., Straniero, O., Piersanti, L., & Gobrecht, D. 2015, *ApJS*, 219, 40

Cunha, K., Smith, V. V., Hasselquist, S., et al. 2017, *ApJ*, 844, 145

Fehlberg, E. 1968, NASA Technical Report, 315

Fernández-Trincado, J. G., Robin, A. C., Moreno, E., et al. 2016a, *ApJ*, 833, 132

Fernández-Trincado, J. G., Robin, A. C., Reylé, C., et al. 2016b, *MNRAS*, 461, 1404

Fernández-Trincado, J. G., Robin, A. C., Vieira, K., et al. 2015a, *A&A*, 583, A76

Fernández-Trincado, J. G., Vivas, A. K., Mateu, C. E., et al. 2015b, *A&A*, 574, A15

Fernández-Trincado, J. G., Zamora, O., García-Hernández, D. A., et al. 2017, *ApJ*, 846, L2

Fernández-Trincado, J. G., Zamora, O., Souto, D., et al. 2018, arXiv e-prints [arXiv:1801.07136]

Fishlock, C. K., Karakas, A. I., Lugaro, M., & Yong, D. 2014, *ApJ*, 797, 44

Gaia Collaboration, Brown, A. G. A., Vallenari, A., et al. 2018, *A&A*, 616, A1

García-Hernández, D. A., García-Lario, P., Plez, B., et al. 2006, *Science*, 314, 1751

García Pérez, A. E., Allende Prieto, C., Holtzman, J. A., et al. 2016, *AJ*, 151, 144

González Hernández, J. I. & Bonifacio, P. 2009, *A&A*, 497, 497

Gunn, J. E., Siegmund, W. A., Mannery, E. J., et al. 2006, *AJ*, 131, 2332

Gustafsson, B., Edvardsson, B., Eriksson, K., et al. 2008, *A&A*, 486, 951

Hansen, T. T., Andersen, J., Nordström, B., et al. 2016, *A&A*, 588, A3

Hasselquist, S., Shetrone, M., Cunha, K., et al. 2016, *ApJ*, 833, 81

Hasselquist, S., Shetrone, M., Smith, V., et al. 2017, *ApJ*, 845, 162

Hawkins, K., Masseron, T., Jofré, P., et al. 2016, *A&A*, 594, A43

Holtzman, J. A., Shetrone, M., Johnson, J. A., et al. 2015, *AJ*, 150, 148

Johnson, J. A., Herwig, F., Beers, T. C., & Christlieb, N. 2007, *ApJ*, 658, 1203

Lennon, D. J., Dufton, P. L., & Crowley, C. 2003, *A&A*, 398, 455

Lind, K., Koposov, S. E., Battistini, C., et al. 2015, *A&A*, 575, L12

Majewski, S. R., Schiavon, R. P., Frinchaboy, P. M., et al. 2017, *AJ*, 154, 94

Majewski, S. R., Zasowski, G., & Nidever, D. L. 2011, *ApJ*, 739, 25

Martell, S. L. & Grebel, E. K. 2010, *A&A*, 519, A14

Martell, S. L., Shetrone, M. D., Lucatello, S., et al. 2016, *ApJ*, 825, 146

Martell, S. L., Smolinski, J. P., Beers, T. C., & Grebel, E. K. 2011, *A&A*, 534, A136

Masseron, T., García-Hernández, D. A., Mészáros, S., et al. 2018, arXiv e-prints [arXiv: 1812.08817]

Masseron, T., Merle, T., & Hawkins, K. 2016, BACCHUS: Brussels Automatic Code for Characterizing High accuracy Spectra, Astrophysics Source Code Library

Mennickent, R. E., Kołaczkowski, Z., Djurasevic, G., et al. 2012, *MNRAS*, 427, 607

Mennickent, R. E., Kołaczkowski, Z., Soszyński, I., Cabezas, M., & Garrido, H. E. 2018a, *MNRAS*, 473, 4055

Mennickent, R. E., Rivinius, T., Cidale, L., Soszyński, I., & Fernández-Trincado, J. G. 2018b, *PASP*, 130, 094204

Mészáros, S., Martell, S. L., Shetrone, M., et al. 2015, *AJ*, 149, 153

Nidever, D. L., Holtzman, J. A., Allende Prieto, C., et al. 2015, *AJ*, 150, 173

Pereira, C. B., Smith, V. V., Drake, N. A., et al. 2017, *MNRAS*, 469, 774

Plez, B. 2012, Turbospectrum: Code for spectral synthesis, Astrophysics Source Code Library

Price-Whelan, A. M., Hogg, D. W., Rix, H.-W., et al. 2018, *AJ*, 156, 18

Queiroz, A. B. A., Anders, F., Santiago, B. X., et al. 2018, *MNRAS*, 476, 2556

Recio-Blanco, A., Rojas-Arriagada, A., de Laverny, P., et al. 2017, *A&A*, 602, L14

Reis, I., Poznanski, D., Baron, D., Zasowski, G., & Shahaf, S. 2018, *MNRAS*, 476, 2117

Schiavon, R. P., Zamora, O., Carrera, R., et al. 2017, *MNRAS*, 465, 501

Shetrone, M., Venn, K. A., Tolstoy, E., et al. 2003, *AJ*, 125, 684

Smith, V. V., Cunha, K., Shetrone, M. D., et al. 2013, *ApJ*, 765, 16

Sneden, C., Cowan, J. J., & Gallino, R. 2008, *ARA&A*, 46, 241

Starkenburg, E., Shetrone, M. D., McConnachie, A. W., & Venn, K. A. 2014, *MNRAS*, 441, 1217

Ting, Y.-S., Conroy, C., Rix, H.-W., & Cargile, P. 2018, arXiv e-prints [arXiv: 1804.01530]

Ventura, P., Stanghellini, L., Di Criscienzo, M., García-Hernández, D. A., & Dell'Agli, F. 2016, *MNRAS*, 460, 3940

Zamora, O., García-Hernández, D. A., Allende Prieto, C., et al. 2015, *AJ*, 149, 181

Zasowski, G., Cohen, R. E., Chojnowski, S. D., et al. 2017, *AJ*, 154, 198

Zasowski, G., Johnson, J. A., Frinchaboy, P. M., et al. 2013, *AJ*, 146, 81

¹ Instituto de Astronomía y Ciencias Planetarias, Universidad de Atacama, Copayapu 485, Copiapó, Chile

e-mail: jfernandezt87@gmail.com and/or jfernandez@obs-besancon.fr

² Institut Utinam, CNRS UMR 6213, Université Bourgogne-Franche-Comté, OSU THETA Franche-Comté, Observatoire de Besançon, BP 1615, 25010 Besançon Cedex, France

³ Departamento de Astronomía, Casilla 160-C, Universidad de Concepción, Concepción, Chile

⁴ Astronomical Institute of the Academy of Sciences of the Czech Republic, Boční II 1401/1, Prague, 141 00, Czech Republic

⁵ Instituto de Astrofísica de Canarias, Vía Láctea S/N, E-38205 La Laguna, Tenerife, Spain

⁶ Departamento de Astrofísica, Universidad de La Laguna (ULL), E-38206 La Laguna, Tenerife, Spain

⁷ School of Physics, University of New South Wales, Sydney NSW 2052

⁸ Centre of Excellence for Astrophysics in Three Dimensions (ASTRO-3D), Australia

⁹ Department of Physics and JINA Center for the Evolution of the Elements, University of Notre Dame, Notre Dame, IN 46556, USA

¹⁰ Center for Astrophysical Sciences and Department of Physics and Astronomy, The Johns Hopkins University, Baltimore, MD 21218

¹¹ ELTE Eötvös Loránd University, Gothard Astrophysical Observatory, Szombathely, Hungary

¹² Premium Postdoctoral Fellow of the Hungarian Academy of Sciences

¹³ Depto. de Cs. Físicas, Facultad de Ciencias Exactas, Universidad Andrés Bello, Av. Fernández Concha 700, Las Condes, Santiago, Chile

¹⁴ Millennium Institute of Astrophysics, Av. Vicuña Mackenna 4860, 782-0436, Santiago, Chile

¹⁵ Vatican Observatory, V00120 Vatican City State, Italy

¹⁶ School of Physics and Astronomy, Sun Yat-sen University, Zhuhai 519082, China

¹⁷ Universidade de São Paulo, IAG, Rua do Matão 1226, Cidade Universitária, São Paulo 05508-900, Brazil;

Appendix A: Line-by-line abundances

Table A.1 and A.2 list the atomic and molecular lines used to derived abundances from a line-by-line differential analysis using the the current version of the Brussels Automatic Stellar Parameter (BACCHUS) code (see [Masseron et al. 2016](#)), which relies on the radiative transfer code Turbospectrum ([Alvarez & Plez 1998; Plez 2012](#)) and the MARCS model atmosphere grid ([Gustafsson et al. 2008](#)). For each element and each line, the abundance determination proceeds as in [Hawkins et al. \(2016\)](#), and summarized here for guidance: (i) A spectrum synthesis, using the full set of (atomic and molecular) lines, is used to find the local continuum level via a linear fit; (ii) cosmic and telluric rejections are performed; (iii) the local S/N is estimated; (iv) a series of flux points contributing to a given absorption line is automatically selected; and (v) abundances are then derived by comparing the observed spectrum with a set of convolved synthetic spectra characterised by different abundances. Four different abundance determinations are used: (i) Line-profile fitting; (ii) a core line-intensity comparison; (iii) a global goodness-of-fit estimate; and (iv) equivalent width comparison. Each diagnostic yields validation flags. Based on these flags, a decision tree then rejects the line or accepts it, keeping the best-fit abundance. We adopted the χ^2 diagnostic for the abundance decision, it is the most robust. However, we store the information from the other diagnostics, including the standard deviation between all four methods. The linelist used in this work is the latest internal DR14 atomic/molecular linelist (linelist.20170418), and the Ce II lines from [Cunha et al. \(2017\)](#). For a more detailed description of these lines, we refer the reader to a forthcoming paper

(Holtzman et al., in preparation). In particular, a mix of heavily CN-cycle and α -poor MARCS models were used, as well as the same molecular lines adopted by [Smith et al. \(2013\)](#), were employed to determine the C, N, and O abundances. In addition, we have adopted the C, N, and O abundances that satisfy the fitting of all molecular lines consistently; i.e., we first derive ^{16}O abundances from ^{16}OH lines, then derive ^{12}C from $^{12}\text{C}^{16}\text{O}$ lines and ^{14}N from $^{12}\text{C}^{14}\text{N}$, lines and the CNO abundances are derived several times to minimize the OH, CO, and CN dependences (see, e.g., [Smith et al. 2013; Fernández-Trincado et al. 2018](#)).

We additionally evaluated the possibility to apply the approach of fixing $T_{\text{eff}}^{\text{pho}}$ and $\log g$ to values determined independently of spectroscopy, in order to check for any significant deviation in the chemical abundances. For this, the photometric effective temperature, $T_{\text{eff}}^{\text{pho}} = 4806.6$ K, was calculated from the $J_{2\text{MASS}} - K_{s,2\text{MASS}}$ color relation using the methodology presented in [González Hernández & Bonifacio \(2009\)](#); for 2M12451043+1217401 we adopt $J_{2\text{MASS}} - K_{s,2\text{MASS}} = 0.637$ mag and $[\text{Fe}/\text{H}] = -1.09$. Photometry is extinction-corrected using the Rayleigh Jeans Color Excess (RJCE) method (see [Majewski et al. 2011](#)), which leads to $\langle A_K^{\text{WISE}} \rangle \sim 0.023$ mag. The resulting temperature, $T_{\text{eff}}^{\text{pho}} = 4806.6$ K, is in very good agreement with the spectroscopic temperatures from ASPCAP and Payne-APOGEE. In conclusion, this small T_{eff} discrepancy does not affect our results. In the following, our analysis is restricted to the atmospheric parameters as listed in Table 1. The same table also lists the abundance measurements in this star obtained with the BACCHUS code and compared to ASPCAP and Payne-APOGEE pipelines. Here, we also list the total error bar on our measurements, which is based on the contributions from the statistical and systematic uncertainties.

Appendix B: Variability

Here we use multi-epoch radial velocity measurements available in the APOGEE-2 DR14 database. 2M12451043+1217401 was observed multiple times in a series of 25 "visits" in order to meet the signal-to-noise ratio requirements of the APOGEE-2 survey. The radial velocities for each visit are determined using an iterative scheme, i.e., the individual visit spectra are combined using initial guesses for the relative radial velocities into a co-added spectrum, which is then used to re-derive the relative visit velocities (see, e.g., [Nidever et al. 2015; Price-Whelan et al. 2018](#)).

Generally, observations from the APOGEE-2 survey have a relatively short ($\lesssim 6$ months) baseline, which is a potential limitation to enable the detection of N-rich stars formed through the binary channel. Here, however, we find that the large scatter ($> 9.92 \text{ km s}^{-1}$) shown by the measured radial velocities in 2M12451043+1217401 implies the clear existence of at least one companion. So far, no evidence of strong radial velocity variations has been found in stars with nitrogen over-abundances in the APOGEE survey (see, e.g., [Martell et al. 2016; Fernández-Trincado et al. 2016a, 2017; Schiavon et al. 2017](#)). Therefore, establishing the presence of radial velocity variation among these stars would be required in order to understand if many, or all such objects, formed through the binary channel.

Although APOGEE-2 observed our star during multiple "visits", we omitted one observation with a signal to noise ratio (SNR) below 4 per pixel from our radial velocity analysis. The observations are summarized in Table B.1, which lists the APOGEE radial velocities, their uncertainties, and the signal-to-noise ratio (SNR) per pixel for each epoch.

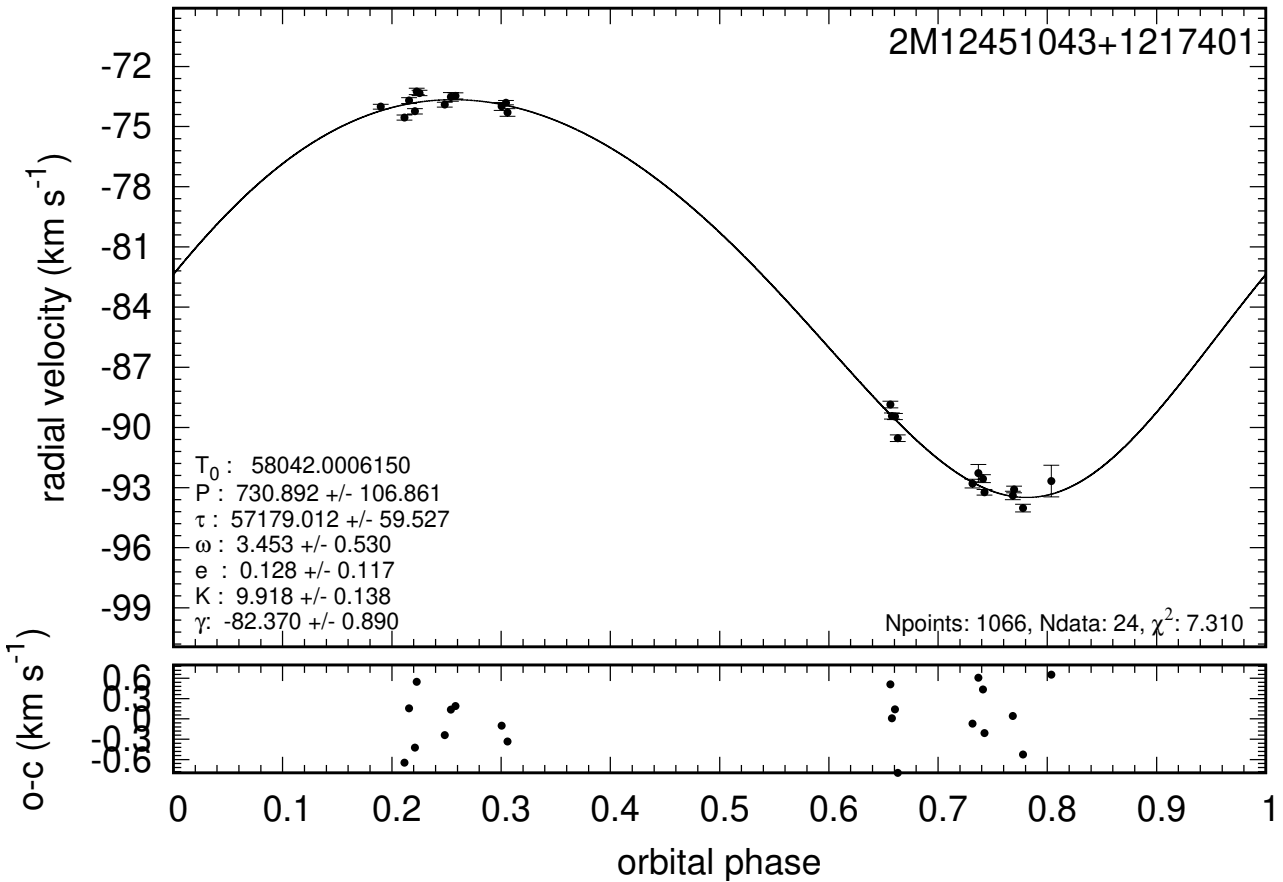


Fig. B.1. Radial velocity measurements for 2MASS J12451043+1217401 from 24 visits of the APOGEE-2 survey (*top panel*) with the best-fit, with the residual velocities (*bottom panel*).

We conducted a search for the orbital period using the genetic algorithm PIKAIA (Charbonneau 1995) to determine the orbital parameters that best fit the available data. Following the analysis described by Mennickent et al. (2012, 2018a,b) we minimize χ^2 defined as:

$$\chi^2(P, \tau, \omega, e, K, \gamma) = \frac{1}{N-6} \sum_{j=1}^n \left(\frac{V_j - V(t_j, P, \tau, \omega, e, K, \gamma)}{\sigma_j} \right)^2, \quad (\text{B.1})$$

where N is the number of observations, and V_j and V are the observed and calculated velocities in time t_j . The fit velocity is:

$$V(t) = \gamma + K((\omega + \theta(t)) + e \cos(\omega)), \quad (\text{B.2})$$

where θ is the true anomaly obtained by solving the equations:

$$\tan\left(\frac{\theta}{2}\right) = \sqrt{\frac{1+e}{1-e}} \tan\left(\frac{E}{2}\right), \quad (\text{B.3})$$

$$E - e \sin(E) = \frac{2\pi}{P}(t - \tau), \quad (\text{B.4})$$

where E is the eccentric anomaly. We constrained the eccentricity between 0 and 1, ω between 0 and 2π , τ between the minimum HJD and this value plus the period, K between 0 and $(V_{\max} - V_{\min})$, and γ between V_{\min} and V_{\max} .

In order to estimate the errors for the results obtained from PIKAIA, we proceeded to calculate the confidence intervals for the region corresponding to 68.26% of the sample (1σ). The results are listed in Table B.2. The fit produces a good match to the available data (residuals $\approx 1 \text{ km s}^{-1}$, see bottom panel in Fig. B.1).

It is important to note that 2MASS J12451043+1217401 was identified as a "bimodal binary" in the bimodal period samplings of *The Joker* code in Price-Whelan et al. (2018), corresponding to periods between $P \approx 650$ –950 days and eccentricity between ≈ 0.07 –0.3: $(P_1, e_1) = (939.80, 0.31)$ days and $(P_2, e_2) = (689.85 \text{ days}, 0.07)$. The best-fit orbital parameters from PIKAIA are an orbital period of 730.89 ± 106.86 days, a velocity semi-amplitude of $9.92 \pm 0.014 \text{ km s}^{-1}$, and an eccentricity of 0.1276 ± 0.1174 . These are in acceptable agreement with the shorter period reported by Price-Whelan et al. (2018).

Visual inspection of the spectrum of 2MASS J12451043+1217401 does not reveal any obvious signs of binary interaction, such as emission lines from an accretion disk. If this is a post-mass-transfer binary system, the primary would have evolved into a white dwarf by this point, making it quite difficult to detect in the H -band. Alternately, if there was very strong mass loss from the primary, the binary system could have disrupted or significantly widened. For the case of SB1 binaries, where only one component is detected in the spectrum, the mass information is

Table A.1. Atomic lines and derived log abundances for the light elements Fe, Al, Mg, and Si, and the heavy element Ce.

Element	$\lambda^{air}(\text{\AA})$	$\log(\epsilon)$
Fe I		
15207.5	6.194	
15245.0	6.317	
15294.6	6.225	
15394.7	6.377	
15500.8	6.210	
15501.3	6.216	
15531.8	6.443	
15534.2	6.415	
15588.3	6.515	
15591.5	6.308	
15604.2	6.180	
15621.7	6.324	
15632.0	6.296	
15662.0	6.332	
15723.6	6.356	
15769.1	6.583	
15769.4	6.583	
15774.1	6.400	
15895.2	6.456	
15904.3	6.419	
15920.6	6.324	
15964.9	6.460	
15967.7	6.414	
15980.7	6.331	
16006.8	6.356	
16007.1	6.357	
16040.7	6.437	
16042.7	6.172	
16071.4	6.453	
16125.9	6.505	
16153.2	6.419	
16179.6	6.379	
16195.1	5.969	
16284.8	6.489	
16517.2	6.402	
16524.5	6.427	
16561.8	6.483	
16645.9	6.300	
16665.5	6.468	
$\langle A(\text{Fe}) \rangle \pm \sigma_{\text{mean}}$	6.37 \pm 0.12	
Al I		
16719.0	5.253	
16750.6	5.237	
16763.4	5.503	
$\langle A(\text{Al}) \rangle \pm \sigma_{\text{mean}}$	5.33 \pm 0.12	
Mg I		
15740.7	6.586	
15748.9	6.556	
15765.8	6.537	
$\langle A(\text{Mg}) \rangle \pm \sigma_{\text{mean}}$	6.56 \pm 0.02	
Si I		
15376.8	6.450	
15557.8	6.629	
15884.5	6.475	
15960.1	6.623	
16060.0	6.738	
16094.8	6.728	
16215.7	6.762	
16241.8	6.775	
16680.8	6.570	
16828.2	6.766	
$\langle A(\text{Si}) \rangle \pm \sigma_{\text{mean}}$	6.65 \pm 0.12	
Ce II		
15784.8	$\langle 1.028 \rangle$	
15958.4	$\langle 1.054 \rangle$	
16376.5	0.871	
$\langle A(\text{Ce}) \rangle \pm \sigma_{\text{mean}}$	0.984 \pm 0.08	

contained in a single function, called the mass function, defined as:

$$f = \frac{(m_1^3)(\sin^3(i))}{(m_1 + m_2)^2} = 1.0361 \times 10^{-7} (1 - e^2)^{3/2} \left(\frac{K_2}{\text{km s}^{-1}} \right)^3 \frac{P_o}{\text{days}} M_{\odot} \quad (\text{B.5})$$

Table A.2. Molecular features and log abundances used to derive C, N, and O.

Element	$\lambda^{air}(\text{\AA})$	$\log(\epsilon)$
^{12}C from $^{12}\text{C}^{16}\text{O}$ lines	15578.0	7.532
	16185.5	7.202
$\langle A(\text{C}) \rangle \pm \sigma_{\text{mean}}$		7.37 \pm 0.17
^{14}N from $^{12}\text{C}^{14}\text{N}$ lines	15158.0	6.980
	15165.4	7.483
	15185.6	7.152
	15210.2	7.228
	15222.0	7.433
	15251.8	7.118
	15284.5	7.494
	15309.0	7.442
	15317.6	7.591
	15328.4	7.226
	15363.5	7.483
	15447.0	7.432
	15462.4	7.400
	15466.2	7.587
	15495.0	7.489
	15514.0	7.420
	15581.0	7.264
	15659.0	7.592
	16244.0	7.507
$\langle A(\text{N}) \rangle \pm \sigma_{\text{mean}}$		7.39 \pm 0.17
^{16}O from ^{16}OH lines	15409.2	8.153
	15568.8	8.003
	16052.8	7.748
	16055.5	7.660
	16255.0	7.935
	16312.6	8.287
	16534.6	7.893
	16650.0	8.149
	16656.0	8.160
	16704.5	8.215
	16898.9	8.153
$\langle A(\text{O}) \rangle \pm \sigma_{\text{mean}}$		8.03 \pm 0.19

Table A.3. Abundance determination sensitivity to the stellar parameters from our present measurements.

$\Delta[\text{X}/\text{H}]$	$T_{\text{eff}} \pm 100 \text{ K}$	$\log g \pm 0.3$	$\xi_t \pm 0.05 \text{ km s}^{-1}$
Fe	0.03	0.05	0.002
C	0.14	0.06	0.002
N	0.11	0.09	0.001
O	0.09	0.03	0.007
Al	0.04	0.04	0.004
Mg	0.08	0.09	0.060
Si	0.02	0.06	0.004
Ce	0.05	0.19	0.002

This corresponds to the minimum mass of the unseen companion, labeled with subscript 1 here, in this case $0.07 M_{\odot}$. Since the system inclination is unknown, several solutions are possible for the mass of the unseen companion. Assuming $1 M_{\odot}$ for the detected star (Price-Whelan et al. 2018), we summarize our restrictions for the mass of the unseen companion in Fig. B.2.

Appendix C: Dynamical behaviour

Here we present a first attempt to predict the probable orbit of the newly discovered N-rich binary across the Milky Way. To do this, we have used a state-of-the art orbital integration model in an (as far as possible) realistic gravitational potential, that fits

Table B.1. APOGEE Observations

Julian date	RV (km s ⁻¹)	σ (km s ⁻¹)	SNR (pixel ⁻¹)
2457059.94391	-88.85	0.16	20
2457060.91321	-89.43	0.15	20
2457062.99631	-89.45	0.15	20
2457064.89865	-90.54	0.17	18
2457114.79574	-92.80	0.22	17
2457118.85652	-92.28	0.43	8
2457121.82661	-92.55	0.19	16
2457122.80708	-93.23	0.14	23
2457141.73865	-93.40	0.21	15
2457142.73487	-93.09	0.17	18
2457148.68704	-94.02	0.19	16
2457167.65509	-92.67	0.79	5
2457449.88122	-74.01	0.12	26
2457465.78237	-74.55	0.12	22
2457468.79933	-73.70	0.14	22
2457472.79234	-74.23	0.14	23
2457473.88693	-73.25	0.16	20
2457475.83189	-73.32	0.13	22
2457492.72504	-73.91	0.12	23
2457496.80519	-73.52	0.21	14
2457499.79405	-73.47	0.16	19
2457504.78284	-69.84	0.89	4
2457530.70246	-73.99	0.19	16
2457533.71368	-73.81	0.11	25
2457534.73149	-74.29	0.19	14

Notes. ^aReduced Heliocentric JD. ^bValues omitted for spectra with SNR < 5.

Table B.2. Orbital elements for the donor of 2M12451043+1217401 obtained by minimization of the χ^2 parameter given by Eq. B.1. The value $\tau^* = \tau - 2450000$ and the limits of the confidence intervals within one standard deviation (1σ) are given.

Parameter	Best value	Lower limit	Upper limit
P_o (d)	730.89 ± 106.86	679.61	893.33
τ^*	57179.0117 ± 59.5272	57129.9301	57248.9845
ω	3.45 ± 0.53 [rad]	2.961	4.022
e	0.1276 ± 0.1174	0.0569	0.2916
K_2 (km s ⁻¹)	9.92 ± 0.14	9.856	10.131
γ (km s ⁻¹)	-82.37 ± 0.89	-83.22	-81.44

the structural and dynamical parameters of the Galaxy based on the recent knowledge of our Milky Way. For the computations in this work, we have employed the rotating "boxy/peanut" bar model of the novel galactic potential model, called GravPot16³, along with other composite stellar components. The considered structural parameters of our bar model, e.g., mass, present-day orientation, and pattern speeds, is within observational estimations that lie in the range of 1.1×10^{10} M_{sun}, 20°, and 35–50 km s⁻¹ kpc, respectively.

For reference, the Galactic convention adopted by this work is: X–axis is oriented toward $l = 0^\circ$ and $b = 0^\circ$, and the Y–axis is oriented toward $l = 90^\circ$ and $b = 0^\circ$, and the disk rotates toward $l = 90^\circ$; the velocity components are also oriented along these directions. In this convention, the Sun's orbital velocity vector are $[U_\odot, V_\odot, W_\odot] = [11.1, 12.24, 7.25]$ km s⁻¹ (Brunthaler et al. 2011). The model has been rescaled to the Sun's Galactocentric distance, 8.3 kpc, and a local rotation velocity of 239 km s⁻¹. For computation of the Galactic orbits, we have a simple Monte

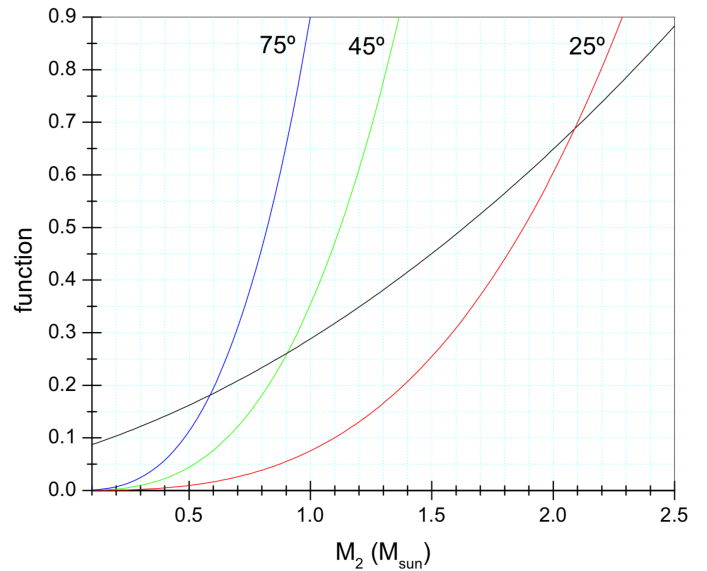


Fig. B.2. From the system mass function (Eq. B.5), and assuming a $1 M_\odot$ for the detected component, we can determine the mass of the unseen companion from the intersection of two functions of the form $m_1^3 \sin^3 i$ and $g(P, K_2, e) \times (m_1 + m_2)^2$, where g is a function of the orbital period, radial velocity half-amplitude, and orbital eccentricity. These functions are plotted for our system for three different angles showing possible ranges of masses for the companion.

Carlo procedure and the Runge-Kutta algorithm of seventh-eight order elaborated by Fehlberg (1968). The uncertainties in the input data (e.g., distances, proper motions, and line-of-sight velocity errors listed in Table C.1) are assumed to follow a Gaussian distribution and were propagated as 1σ variations in a Gaussian Monte Carlo re-sampling. We have sampled a half million orbits, computed backward in time for 3 Gyr. Fig. C.1 shows the probability densities of the resulting orbits projected on the equatorial (left column) and meridional (right column) Galactic planes, in the non-inertial reference frame where the bar is at rest. The orbital path (adopting central values) is shown by the black line in the same figure. The green and yellow colours correspond to more probable regions of the space, which are crossed more frequently by the simulated orbits.

We derive the distance to 2M12451043+1217401 using StarHorse⁴, a Bayesian distance estimator initially developed for APOGEE stars (Queiroz et al. 2018). For completeness, we provide dynamical solutions and orbit calculations for both the StarHorse distance of 13 kpc and the Bailer-Jones et al. (2018) distance of 4.5 kpc. The two columns on the left of Fig. C.1 shows possible orbits given the StarHorse distance and different bar speeds (35, 40, 45 and 50 km s⁻¹ kpc), and the two columns on the right show the same figures for the Bailer-Jones et al. (2018) distance.

³ <https://fernandez-trincado.github.io/GravPot16/>

⁴ https://data.sdss.org/sas/dr14/apogee/vac/apogee_tgas/apogee_tgas-DR14.fits

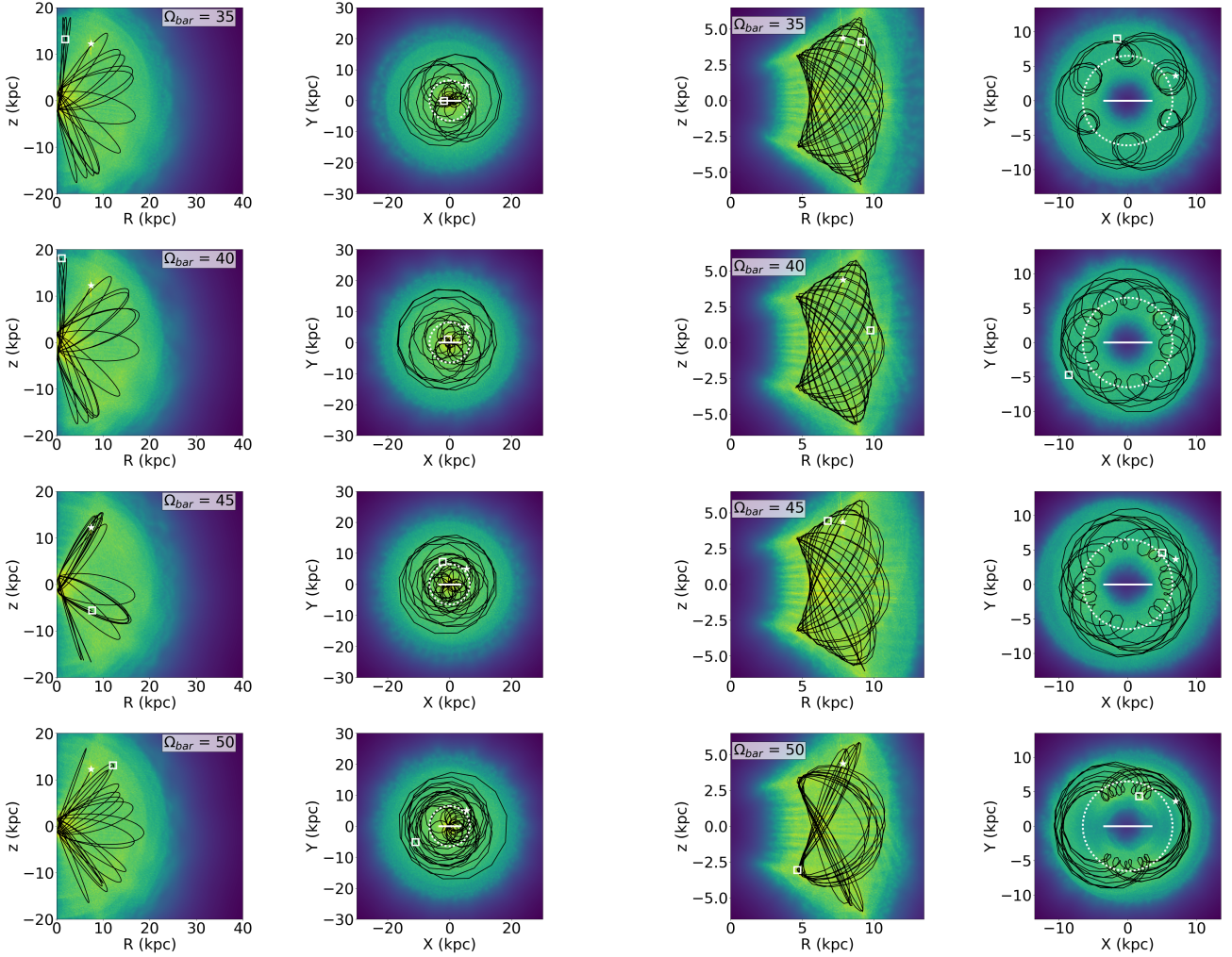


Fig. C.1. Kernel Density Estimate (KDE) smoothed distribution of simulated orbits employing a Monte Carlo approach, showing the probability densities of the resulting orbits projected on the equatorial and meridional Galactic planes in the non-inertial reference frame where the bar is at rest. The green and yellow colors correspond to more probable regions of the space, which are crossed more frequently by the simulated orbits. The black line is the orbit of 2M12451043+1217401 adopting the central inputs. The small white star marks the present position of the cluster, whereas the white square marks its initial position. In all orbit panels, the white dotted circle show the location of the co-rotation radius (CR), the horizontal white solid line shows the extension of the bar. Columns 1 and 2 show the results adopting the estimated distance from the StarHorse code, while columns 3 and 4 for estimated distance from [Bailer-Jones et al. \(2018\)](#).

Table C.1. Phase-space data

Coordinates	(J2000)
(α, δ)	(191°.293486, 12°.294486)
(l, b)	(296°.973729363, 75°.0936328462)
Heliocentric Distance	[kpc]
	(4.54 ± 0.93) ^a
	(13.02 ± 1.49) ^b
$\langle RV \rangle \pm \sigma_{RV}$	[km s ⁻¹]
	(-82.8±9.9) ^c
Proper Motions	($\mu_\alpha \cos \delta$, μ_δ)
	[mas yr ⁻¹]
	(-1.32 ± 0.12, -4.19 ± 0.06) ^d

Notes. ^a Estimated distance computed by [Bailer-Jones et al. \(2018\)](#); ^b Estimated distance computed using the StarHorse code ([Queiroz et al. 2018](#)); ^c The average radial velocity of the binary system computed from the 24 visits of the APOGEE/DR14 spectra (see text); ^d Absolute proper motions from [Gaia Collaboration et al. \(2018\)](#).